ACS APPLIED NANO MATERIALS
Cite This: ACS Appl. Nano Mater. 2018, 1, 1175−1187
Article
www.acsanm.org

Functionalized Self-Assembled Peptide Nanotubes with Cobalt Ferrite Nanoparticles for Applications in Organic Electronics

Soma Khanra,[†] Md Abdullah-Al Mamun,[‡] Fabio F. Ferreira,[§] Kartik Ghosh,[‡] and Suchismita Guha*[,†]

[†]Department of Physics and Astronomy, University of Missouri, Columbia, Missouri 65211, United States
[‡]Physics, Astronomy, and Materials Science, Missouri State University, Springfield, Missouri 65897, United States
[§]Center for Natural and Human Sciences (CCNH), Federal University of ABC (UFABC), Av. dos Estados, 5001, 09210-580, Santo André, São Paulo, Brazil

Supporting Information

ABSTRACT: Here, we report the functionalization of diphenylalanine (FF)-based self-assembled nanotubes with cobalt ferrite (CFO) magnetic nanoparticles. Electron microscopy images show the CFO nanoparticles to be uniformly dispersed on the peptide nanotubes. We investigate the interaction between CFO nanoparticles and FF nanotubes by optical spectroscopy, X-ray photoelectron spectroscopy (XPS), and magnetization measurements. The changes in the XPS data from pristine FF nanotubes and CFO:FF nanotubes are indicative of charge transfer from CFO to FF nanotubes, changing the electronic states of the Fe^{2+} and Co^{2+} ions. The A_{1g} Raman peak of CFO at 675 cm^{-1} hardens in CFO:FF nanotubes, signaling an enhancement of the stiffness constant of the iron−oxygen bond due to charge transfer. A comparison of the magnetic characterization from CFO nanoparticles and the CFO:FF nanocomposite shows a higher saturation magnetization from the nanocomposite, which is attributed to a change in the cationic distribution in CFO upon binding with the peptide. The functionalized FF nanotubes open up applications in organic electronics, specifically in low-operating voltage pentacene field-effect transistors.

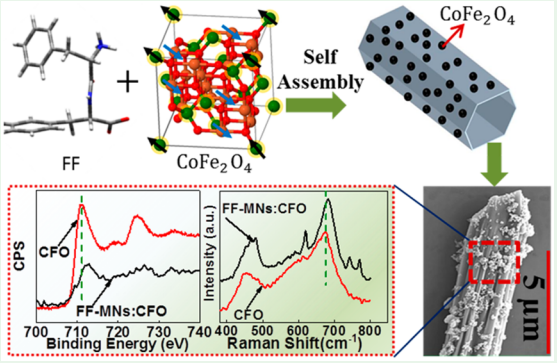

KEYWORDS: *peptide micro/nanostructures, self-assembly, cobalt ferrite, nanobio interaction, Raman spectroscopy, FTIR, magnetization, field-effect transistor*

1. INTRODUCTION

The 21st century revolution in nanobiotechnology is strongly linked to the discovery of new functional materials, which are based on biomolecular nanostructures and inorganic nanoparticles. Self-assembling phenylalanine peptides adopt into various nanostructures, making them ideal as building blocks for directing the growth and assembly of inorganic nanoparticles. These peptide nanostructures are inherently semiconducting, paving the way for applications in eco-friendly optical and electronic applications.[1] *L*,*L*-diphenylalanine (FF), a short peptide made from the covalent link of two aromatic *L*-phenylalanine units, has amphiphilic properties that result in self-organization. The formation of elongated structures with hierarchical order, introduced by the self-assembly process, adds to their mechanical strength[2,3] and thermal stability[4] and makes them attractive in electronic device applications.[5,6]

The self-assembly process in FF-micronanostructures (FF-MNS) has been discussed in several references.[7,8] The process begins with the self-association of six FF monomers into a macrocycle structure with the amino and the carboxyl groups constituting the inner core. The stacking of the macrocycles results in narrow channels forming a hexagonal packing pattern.[9] Eventually, the self-assembly achieves higher ordering where nanotubes form fibrillar bundles. External electric fields may also impact the hierarchical self-assembly process in FF-MNS.[10]

Considering that the self-assembly process in short peptides results from various intermolecular and intramolecular interactions—van der Waals, electrostatic, hydrogen bonds, and hydrogen bonds combined with hydrophobic interaction[11]—the interface between peptide nanostructures and inorganic nanoparticles may be quite complex as this interaction is governed by dynamic forces and thermodynamic exchanges.[12,13] Protein/peptide adsorption and their unfolding properties strongly depend upon the size of the nanoparticles to which they attach.[14] FF-MNS has been shown to be an excellent template for tethering Ag and Au nanoparticles for surface-enhanced Raman scattering.[15,16] Peptide nanostructures also serve as a biodegradable scaffold with π-conjugated polymers as active layers in light-emitting diodes; the

Received: December 13, 2017
Accepted: February 23, 2018
Published: February 23, 2018

DOI: 10.1021/acsanm.7b00344
ACS Appl. Nano Mater. 2018, 1, 1175−1187

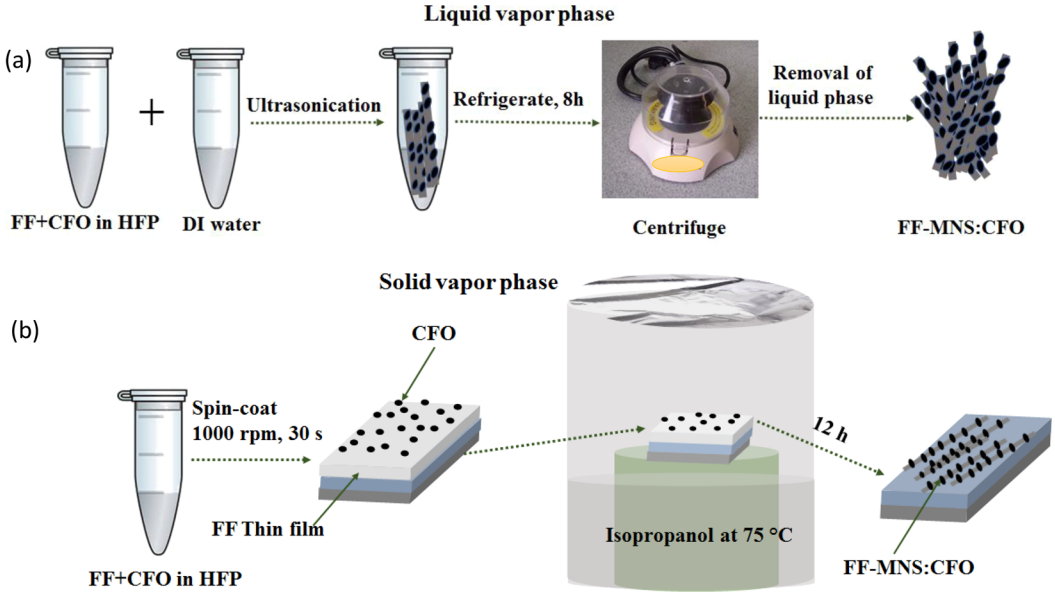

Figure 1. Schematic of the (a) liquid vapor and the (b) solid vapor method for the preparation of FF-MNS:CFO.

peptide−polymer interaction mainly arises from van der Waals force.[6]

Among magnetic nanoparticles, cobalt ferrite ($CoFe_2O_4$ or CFO) has received a lot of interest. Due to its moderate values of saturation magnetization, high magneto-crystalline anisotropy, high Curie temperature, and easy tunability of particle size,[17] it has been utilized in biomedical applications.[18−20] Some studies have shown that a low concentration of CFO is nontoxic for cancer cells.[21] A question that may be raised is whether the magnetization of CFO can be tuned by binding to nontoxic materials such as bioinspired nanostructures. Not only will such a strategy provide a path toward eco-friendly magnetic materials but will also provide a tuning knob for controlling the magnetic properties. Moreover, the insulating properties of CFO are attractive in utilizing it as a gate dielectric in organic thin film transistors, setting the stage for magnetic field controlled transistors and devices.[22]

This work is motivated by a study showing that Co_3O_4 nanoparticles bind to vertically aligned FF nanostructures, opening up possibilities for energy storage.[23] However, thus far there is no study that elucidates the exact nature of interaction between magnetic nanoparticles and peptide nanostructures. We report on the synthesis of functionalized FF-MNS with CFO nanoparticles using the liquid and solid vapor phase method. The FF-MNS:CFO samples were characterized by X-ray diffraction (XRD), scanning/transmission electron microscopy, X-ray photoelectron spectroscopy (XPS), magnetization measurements, and optical spectroscopy. The XPS data clearly show an electrostatic binding between the amine group in FF-MNS and Fe^{2+}/Co^{2+} ions in CFO; the charge transfer is inferred from the change in the binding energy of the Fe ion peak in CFO and the nanocomposite sample, FF-MNS:CFO. The charge transfer between FF-MNS and CFO is also reflected in Raman scattering and FTIR absorption. Further, changes in the magnetic properties are also observed. The saturation magnetization in FF-MNS:CFO is enhanced compared to pristine CFO nanoparticles, which is attributed to a change in the electronic state of Fe and Co ions upon binding with the peptide. As an application in electronics, we show that FF-MNS:CFO used as a dielectric layer in pentacene metal−insulator-semiconductor (MIS) capacitors results in a higher value of capacitance compared to using only FF-MNS as the dielectric layer. Concomitantly, the usage of FF-MNS:CFO as an insulating layer in pentacene field-effect transistors (FETs) lowers the operating voltage compared to only FF-MNS. There are indications that the capacitance may be further tuned using an external magnetic field.

The structure of the paper is as follows. Section 2 provides the experimental methods and methodologies. Sections 3.1 and 3.2 highlight the structure of FF-MNS:CFO using both X-ray diffraction and electron microscopy. To obtain insights into the interaction between FF-MNS and CFO, detailed XPS results are provided in section 3.3. This is followed by Raman scattering and FTIR results in section 3.4; the observed changes in the vibrational spectra of FF-MNS and FF-MNS:CFO highlight the mechanism of the charge transfer process. The magnetization properties of CFO and FF-MNS:CFO are compared in section 3.5, followed by a discussion in section 3.6 as to why the saturation magnetization in FF-MNS:CFO is enhanced compared to only CFO. The FF-MNS:CFO nanocomposite forms a superior dielectric, and its application in pentacene FETs is presented in section 3.7. This is followed by concluding remarks.

2. EXPERIMENTAL METHODS

2.1. Growth and Device Fabrication. *Liquid Vapor Method.* The FF-MNS:CFO powder sample was synthesized using the liquid phase method. In the liquid phase method, 10 mg of FF (purchased from Sigma-Aldrich Inc.) and 4 mg of CFO (purchased from Inframat Advanced Materials, Product # 26F27-ON1, and with an average particle size of 30−40 nm) were first dissolved in 100 μL of 1,1,1,3,3,3-hexafluoro-2-propanol (HFP), and then the mixtures were diluted using 450 μL of DI water. This diluted mixture was immediately ultrasonicated using a probe type ultrasonic homogenizer (Qsonica, Model Q55) at room temperature for 40 s at a 10 kHz frequency. The mixture was then kept in a refrigerator for about 8 h for aggregation and was centrifuged using a Fisher Scientific mini-centrifuge (#05−090−100) at 6600 rpm for about 2 min to separate the solid and liquid phases. Centrifuging eliminates weakly bound CFO nanoparticles to FF-MNS, and as a result the wt % of CFO in the nanocomposite material will be less than the original amount. The liquid phase was removed by a pipet from the separated solid−liquid mixture, and the

DOI: 10.1021/acsanm.7b00344
ACS Appl. Nano Mater. 2018, 1, 1175−1187

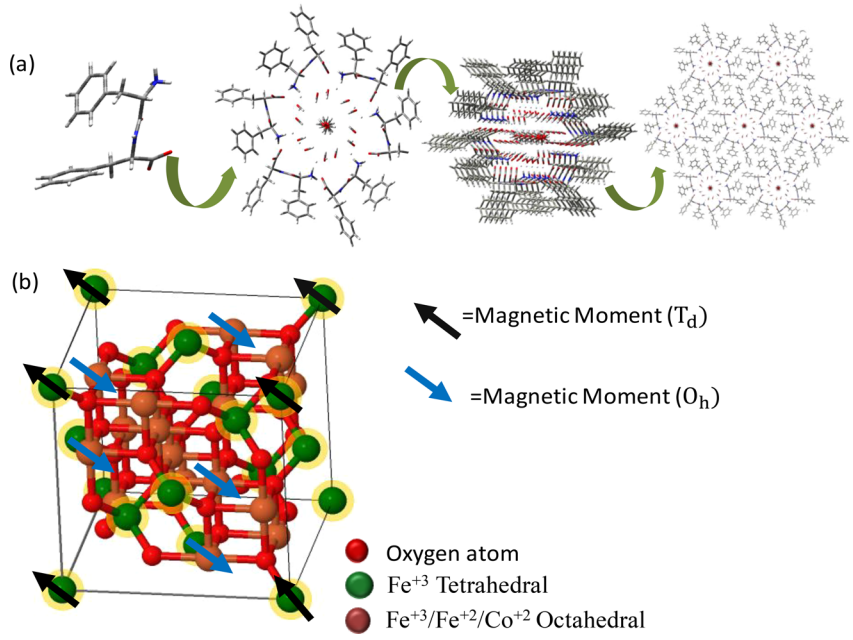

Figure 2. (a) Schematic illustration of the self-assembly process in FF, starting with the dipeptide and forming a 6-fold macrocycle. The macrocycles form a hexagonal sheet. (b) The unit cell of CFO where Fe^{3+} atoms occupy both the octahedral (O_h) and tetrahedral (T_d) sites. The octahedral sites are also occupied by Fe^{2+}, which are replaced by Co^{2+} in CFO. The black and the blue arrows point to the direction of the magnetic moment at the T_d and O_h sites, respectively.

solid phase was kept in an oven at 75 °C until dry. All measurements were performed from such powder samples. A similar procedure was followed for pure FF-MNS synthesis.

Solid Vapor Method. The solid vapor method was used to form thin films of FF-MNS. For FF-MNS:CFO films, 10 mg of FF and 4 mg of CFO were first dissolved in 100 μL HFP solution. A total of 50 μL of this mixture was then spin-coated at 1000 rpm for 30 s on 1″ × 1″ aluminum coated glass slides. Aluminum was thermally evaporated on a glass slide with a thickness of ∼60 nm. The spin-coated FF-MNS films were then placed on an elevated platform in an uncovered Petri dish that contained 20 mL of isopropanol such that only the vapor reached the film. The entire setup was covered with aluminum foil and placed on a hot plate at 80 °C. The incubation time was 720 min. The procedure was identical for synthesizing pure FF-MNS nanostructured thin films. These films were used as dielectric layers for the organic devices. The preparations of the solid and liquid vapor phase methods are schematically shown in Figure 1.

Device fabrication. Bottom-gate top-contact architectures were used for the pentacene FETs and MIS capacitors, similar to ref 5. First, the dielectric films (FF-MNS or FF-MNS:CFO) were deposited using the solid vapor method. For the FETs, a thin layer (<10 nm) of poly(4-vinylphenol) was spin-coated prior to the deposition of FF-MNS/FF-MNS:CFO. Pentacene was then thermally evaporated (0.3 Å/s, 10^{-5} mbar) with a thickness of 60 nm on the dielectric layer. This was followed by thermal evaporation of a 50-nm-thick layer of gold through a shadow mask containing both FET and MIS capacitor structures for the top contacts.

2.2. Characterization. *Raman and Infrared Spectroscopy.* The Raman spectra were collected by an Invia Renishaw spectrometer attached to a microscope with a ×50 lens. The system is equipped with two lasers—a 785 nm diode laser and an argon ion laser with 514 nm as the excitation source. The Raman spectra were collected using the 514 nm excitation source at room temperature. The infrared absorption spectra were collected by a Fourier Transform Infrared (FTIR) spectrometer (ATI, Mattson Infinity Series) using the infrared light source in reflection mode.

X-Ray Diffraction. X-ray data were collected using a STADI-P powder diffractometer (Stoe, Darmstadt, Germany) in transmission geometry by using—depending on the case—Kα1 (λ_{Mo} = 0.7093 Å or λ_{Cu} = 1.54056 Å) wavelengths emitted by Mo and Cu anodes, respectively, and selected by curved Ge(111) crystals. The samples were packed between two 0.014 mm acetate-cellulose foils, which were held spinning during data collection. The diffracted intensities were collected by silicon microstrip detectors, Mythen 1K (Dectris, Baden, Switzerland), in the range from 7.000° to 70.945° (MoKα1), with 100 s of integration time at each 0.78° for the CFO system alone and in the range from 3.000° to 62.835° (Cu Kα1), with 100 s of integration time at each 1.05° for the FF-CFO system.

Transmission Electron Microscopy (TEM) and Scanning Electron Microscopy (SEM). The TEM images were measured with an FEI Tecnai F30 operated at 300 kV. CFO nanoparticles or FF-MNS:CFO were dissolved in methanol and then dispersed onto an ultrathin carbon-coated Cu TEM grid.

The SEM images were obtained using an FEI Quanta 200S equipped with an energy dispersive X-ray analysis (EDS) system. Synthesized FF-MNS:CFO samples were first dissolved in methanol and then drop-casted on glass slides, which were kept on a hot plate at 60 °C in the air until the sample was dry. A thin layer (∼2 nm) of gold was sputtered onto the sample. Grounding of the sample to the sample holder of the SEM was achieved by using copper tapes.

X-Ray Photoelectron Spectroscopy. The XPS data were collected using a Thermo Scientific Alpha 110 hemispherical analyzer with pass energy of 25 eV. Twin crystal monochromatic Al K-alpha with a characteristic energy of 1486.6 eV was used as a source of X-rays. The Ag $3d_{5/2}$ (FWHM = 0.36 eV) peak with a characteristic energy of 368.26 eV was used for calibration of the source and analyzer. Data analysis and peak fitting of the XPS spectra were done using Casa XPS 2.3.16 software. The carbon peak at 284.8 eV was used for the calibration of the XPS data. Shirley background was used for the fitting of the high resolution data. The experimental data were fitted with a combination of Lorentzian and Gaussian line profiles.

Magnetic Characterization. Temperature and magnetic field dependent magnetization data were collected using a SQUID magnetometer (MPMS-XML5, Quantum Design). Magnetization studies were conducted from powder samples at room temperatures until 50 kOe.

Device Characterization. Electrical characterizations were performed at room temperature using Keithley2400 and Keithley236 sourcemeters, configured together by a program written in LabVIEW. Capacitance versus voltage (C−V) characteristics was measured using

DOI: 10.1021/acsanm.7b00344
ACS Appl. Nano Mater. 2018, 1, 1175−1187

an HP 4284A LCR meter. A small DC bias of 200 mV was applied during the measurement. For the magnetic field dependent C−V measurements, a small circular disk magnet with a magnetic field of 0.2 T and magnetization direction along the axis (poles on flat end) was placed under the device. The C−V measurements were performed at 5 kHz.

3. RESULTS AND DISCUSSION

3.1. Structure. Figure 2a shows a schematic of the self-assembly process, starting with the dipeptide. The core of the nanotubes forms porous sheets with two-dimensional hexagonal symmetry as discussed in several other references in detail.[6,24] In the first stage of the self-assembly process, six dipeptide molecules along with a few water molecules form a macrocycle, which eventually forms a sheet with hexagonal symmetry. Several sheets stack together, mainly via the β-sheet interaction, and then roll to form tubes. Theoretical calculations predict roughly 21 water molecules within the FF hexamer for a minimum binding energy configuration.[25] All samples in this work were in the hexagonal phase, which was further confirmed by XRD.

As the intensity of the XRD pattern depends on the atomic scattering factor[26] of all elements contained in a sample, among other factors, we first characterized the CFO system by using a Mo source to minimize fluorescence, typically observed when using a Cu source and studying samples containing elements with K-edge absorptions close to the Cu target of the tube (Co K edge = 7.709 keV; Fe K edge = 7.112 keV; Cu K edge = 8.979 keV). We characterized the CFO sample as having an inverse spinel structure by using the Rietveld method,[27,28] as shown in Figure S1 (Supporting Information). The refined unit cell parameters as well as statistical factors (goodness-of-fit indicator and *R*-factors[29]) were a = 8.3671(8) Å, χ^2 = 1.147, R_{wp} = 9.838%, and R_{Bragg} = 2.137%.

Using a Cu source, we characterized the FF-MNS:CFO powder by using the *L*,*L*-diphenylalanine structure described by Bianchi et al.[30] and the aforementioned CFO structure. The result is shown in Figure S2. Quantitative phase analysis[31] using the Rietveld method revealed a phase mixture of 80.0 ± 0.4 wt % of FF-MNS and 20.0 ± 0.3 wt % of CFO. This result is in accordance with the XPS data as well. The refined unit cell parameters and statistical factors are a(FF) = 24.1251(4) Å, c(FF) = 5.4464(1) Å, a(CFO) = 8.3684(3) Å, χ^2 = 1.416, R_{wp} = 2.762%, $R_{Bragg\text{-}FF}$ = 2.384%, and $R_{Bragg\text{-}CFO}$ = 0.505%. These results clearly show that the FF-MNS is in the hexagonal phase. Although XRD cannot quantify the actual valence of the ions, the structure predicts the presence of Co and Fe ions both in the octahedral and tetrahedral sites.

Several minerals found in nature belong to the spinel group. The spinel structure has a cubic unit cell with 56 atoms, 32 oxygen anions distributed in a cubic close packed structure, and 24 cations (of A^{2+} and B^{3+} type) occupying eight of the 64 available tetrahedral (T_d) sites and 16 of the 32 available octahedral (O_h) sites. In the perfect inverse spinel structure, half of the B^{3+} occupy the T_d sites, and eight A^{2+} ions and eight B^{3+} ions occupy the O_h sites. CFO belongs to the magnetism-engineered iron oxide (Fe_3O_4) with ferrimagnetic spin structure (partially inverse spinel) with O_h and T_d sites, as represented in Figure 2b. The O_h and T_d sites are represented by brown and green atoms, respectively. Fe^{2+} and Fe^{3+} ions occupying the O_h sites align parallel to an external magnetic field, and Fe^{3+} ions in the T_d sites of the FCC-packed oxygen lattice sites are aligned antiparallel to the field.[18] The total magnetic moment of $(Fe^{3+})_{T_d}(Fe^{2+}Fe^{3+})_{O_h}O_4$, thus, arises from the high spin state of Fe^{2+} (with $3d^6$ electronic configuration) in the O_h state as the spin of the Fe^{3+} (O_h) and Fe^{3+} (T_d) ions cancel out. The Co ions in CFO predominantly occupy the O_h site, replacing the Fe^{2+} ions. The effective Bohr magneton is given by $g[J(J+1)]^{1/2}$, where J is the total angular momentum and g is the Landé g factor. Therefore, the magnetic moments (μ_B) per ion for Fe^{3+} ($3d^5$), Fe^{2+} ($3d^6$), and Co^{2+} ($3d^7$) are 5.92, 4.90, and 3.87, respectively. If CFO was a perfect inverse spinel structure, where all Fe^{2+} ions are replaced by Co^{2+} ions, one would expect the magnetic moment per formula unit to be 3.87 since the moments due to Fe^{3+} at the T_d and O_h sites would cancel each other. Typically, in CFO, one finds the saturation magnetization to be higher or lower than the ideal value of 3.87, suggesting that Co ions may also occupy the T_d site and some Fe^{2+} ions are still available at the O_h site. Our Rietveld analysis of CFO shows about 70% of Co^{2+} ions are in the O_h site.

3.2. TEM and SEM. Figures 3a−d show the high resolution TEM (HRTEM) images of CFO nanoparticles at various magnifications. These images show high crystallinity of the CFO nanoparticles. Figure 3e and f are the HRTEM images from a FF nanotube with CFO nanoparticles, and g and h are the SEM images of a FF nanotube and a FF nanotube with CFO, respectively. Although there is some aggregation, the CFO nanoparticles are seen to be distributed all over the tube. The EDS spectra (which were calibrated using Al, Cu, and Au) were also analyzed (Figure S3) at several locations of the FF nanotube with CFO, and they confirm the stoichiometry of cobalt ferrite to be $CoFe_2O_4$.

By comparing the HRTEM image (Figure 3f) with the XRD data, we obtain the lattice spacing of CFO in FF-MNS:CFO. For the (220) plane in pure CFO, a lattice constant of a = 8.367 Å is obtained from the XRD data, which translates into a d spacing of 0.3 nm. The HRTEM results of FF-MNS:CFO yield an identical d spacing of 0.3 nm for CFO, suggesting that there are no changes in the lattice constants in CFO after it binds with FF-MNS.

3.3. XPS Analysis. The XPS survey spectra of FF-MNS, CFO, and FF-MNS:CFO are shown in Figure S4. The spectra confirm the presence of various elements and their weight fraction in the samples. Quantification of the elements in the survey spectra of FF-MNS, FF-MNS:CFO, and CFO further confirms that the wt % of CFO in FF-MNS:CFO is roughly 20−35%, similar to what was found by XRD measurements. High resolution spectra were obtained for C 1s, N 1s, O 1s, Fe 2p, and Co 2p peaks. The binding energies were estimated by fitting the high resolution peaks in the XPS data with an average error bar of ±0.2 eV.

Figure 4 shows the high resolution XPS peaks along with their deconvolution of C 1s, N 1s, and O 1s in FF-MNS and FF-MNS:CFO. The deconvolution of the C 1s peak in the XPS spectra of FF-MNS and FF-MNS:CFO results in four peaks. The lowest energy peak of 282.4 eV may be attributed to environmental contamination. The energies of 284.8, 286.9, and 290.2 eV in FF-MNS are assigned to C−C, C−N or C═O, and O−C═O bonds, respectively. Curve fitting of the C 1s peak in FF-MNS:CFO yields peaks with binding energies of 284.8, 286.2, and 288.6 eV. The N 1s spectrum in FF-MNS was fitted with two peaks centered at 399.9 and 402.4 eV, attributed to the −N−C− bond and the NH_3 bond, respectively. These peaks are seen to shift to lower energies in FF-MNS:CFO with corresponding energies of 398.9 and 400.9 eV. The

DOI: 10.1021/acsanm.7b00344
ACS Appl. Nano Mater. 2018, 1, 1175−1187

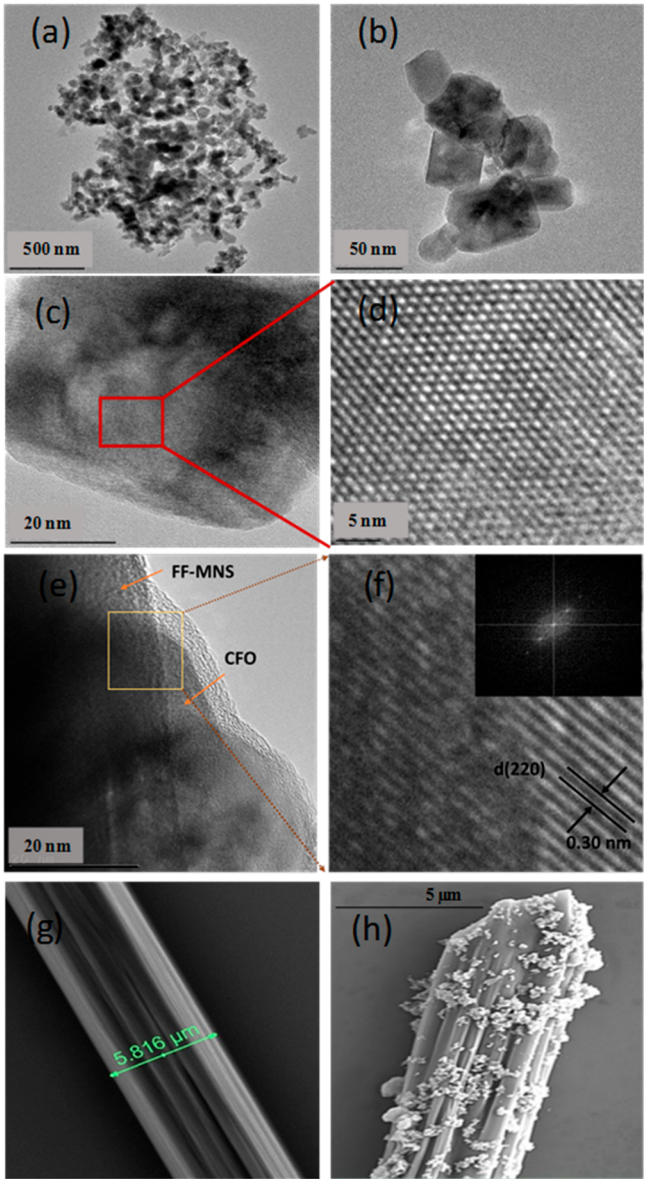

Figure 3. (a–d) TEM images of CFO nanoparticles at various magnifications. (e) High resolution TEM image of FF-MNS:CFO. The yellow box shows the interface between CFO and FF-MNS:CFO, and its magnified image, with lattice fringes, is shown in f. The inset is the Fourier transform of the image. (g) SEM image of a FF nanotube. (h) SEM image of a FF nanotube with CFO.

deconvolution of the O 1s XP spectrum results in four peaks in FF-MNS and three peaks in FF-MNS:CFO. The peak positions in FF-MNS are at 530.3, 531.5, 533.2, and 535.6 eV, which correspond to the binding energies of C–O, C═O or lattice oxygen, hydroxyl group, and chemisorbed oxygen or water, respectively. Although the highest energy peak at 535.6 eV is not observed in FF-MNS:CFO, the binding energies of the other oxygen related peaks do not change. The binding energies obtained by fits to the C 1s, N 1s, and O 1s from FF-MNS and FF-MNS:CFO are tabulated in Table 1. The largest changes in FF-MNS upon binding with CFO are in the binding energies of the amide bond (including the carbonyl bond) and the amine group, suggesting a charge transfer from CFO.

We further analyzed the Fe 2p peaks in FF-MNS:CFO and CFO to obtain the binding energies related to Fe^{3+}/Fe^{2+} ions at the T_d and O_h sites of the lattice. The high resolution Fe 2p spectra are shown in Figure 4d, and the binding energies obtained by fits to the Fe 2p XPS data are listed in Table 1. The Fe 2p XPS data mainly show two peaks centered at 710 and 725 eV. The low energy Fe $2p_{3/2}$ peak in CFO is fitted with two peaks centered at 710.2 and 712.8 eV, which are related to Fe^{3+} ions at the O_h site and T_d site.[32,33] Some works have attributed one of the $2p_{3/2}$ to Fe^{2+} at the O_h site to the coexistence of two valence states of Fe.[34] Our results clearly show an enhancement of the Fe^{3+}/Fe^{2+} binding energy in FF-MNS:CFO. Both CFO and FF-MNS:CFO samples show a satellite peak at roughly 718 eV. The Fe $2p_{1/2}$ peak with a binding energy of 724.3 eV for Fe^{3+} (O_h site) along with a satellite peak at 732.5 eV appears at the same position in FF-MNS:CFO and CFO.

Chemical shifts in binding energies suggest an electronic redistribution or a charge transfer upon the conjugation of two materials. For the interpretation of shifts in binding energies, the general rule is that the binding energy of the central atom increases as the electronegativity of the attached atoms or groups increases.[35] We observe a negative binding energy shift for the C 1s peak. The 286.9 and 290.2 eV peaks in FF-MNS are downshifted to 286.2 and 288.6 eV in FF-MNS:CFO. On the other hand, a positive binding energy shift is observed for the Fe $2p_{3/2}$ spectra; the 712.8 eV peak in CFO shifts to 714.5 eV in FF-MNS:CFO. This is a clear signature of a charge transfer between the Fe ion and C═O and O–C═O bonds in FF, keeping in mind that both O and N atoms (in the peptide) are more electronegative compared to Fe. Hence, the increase in binding energy of the Fe $2p_{3/2}$ peak suggests that an electron is donated to the peptide. This is only possible from Fe^{2+}, which readily oxidizes to Fe^{3+}. These results further suggest that not all the Co ions occupy the O_h site. Since C is more electronegative than Fe according to Pauling's electronegativity table, one would expect the core level of C to shift toward low binding energy and the core level of Fe to shift toward high binding energy. The chemical shifts in the XPS spectra confirm the nature of the charge transfer between FF-MNS and CFO, where the amine group accepts a negative charge from Fe^{2+} in CFO, which further affects the carboxyl group. The XPS Co peaks also shift toward higher binding energies in FF-MNS:CFO compared to pristine CFO (shown in Figure S4). As the signal-to-noise ratio is high for the nanocomposite sample, fitting this region becomes difficult, although one observes an increase in the binding energy, further suggesting a negative charge transfer from Co^{2+} to FF-MNS.

The implications of the electrostatic interaction and the charge transfer between CFO and FF-MNS are many fold. The conjugation of bioinspired materials with CFO or other magnetic nanoparticles may change the inherent magnetization properties at the bio-nano interface, opening applications in biomedicine and electronics. Before discussing the magnetization results, we first discuss our Raman scattering and FTIR results from FF-MNS and FF-MNS:CFO, further shedding insights into the mechanism of interaction between FF-MNS and CFO.

3.4. Raman Scattering and FTIR. The spinel structure of ferrites shows 39 vibrational modes, out of which six phonon modes are Raman active ($2A_{1g}$, E_g, and $3T_{2g}$). The A_{1g} mode, at 680 cm^{-1}, in CFO corresponds to a symmetric stretch of the O atoms along the Fe/Co–O bond. From a detailed work on ferrites and chromites, the A_{1g} mode seems to depend more on the O_h ions than T_d ions.[36] The Raman spectra from FF-MNS, CFO, and FF-MNS:CFO are shown in Figure S5. Details of the

DOI: 10.1021/acsanm.7b00344
ACS Appl. Nano Mater. 2018, 1, 1175–1187

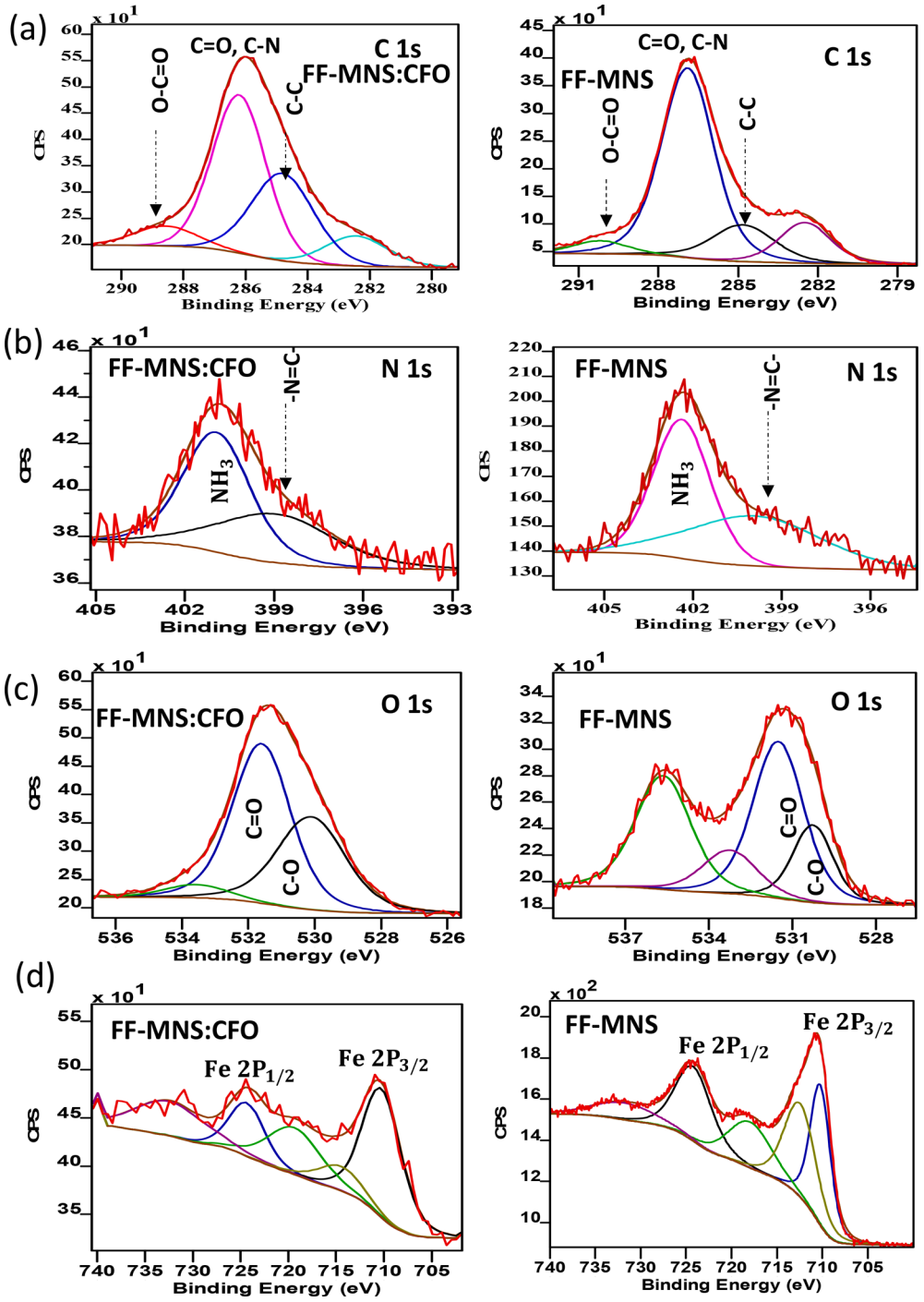

Figure 4. High-resolution X-ray photoelectron spectra of (a) C 1s, (b) N 1s, and (c) O 1s from FF-MNS:CFO (left panel) and FF-MNS (right panel), and (d) Fe 2p in FF-MNS:CFO (left panel) and CFO (right panel).

displacement pattern of the vibrational modes in FF-MNS are found in refs 37 and 38. The Raman spectrum of FF-MNS:CFO shows characteristic features both from FF-MNS and CFO. Comparing the Raman peak positions of the nanocomposite sample to pristine FF-MNS and CFO allows an understanding of how the chemical bonds are affected.

To highlight the changes, we show two regions in Figure 5: the 400−700 cm^{-1} and 1300−1500 cm^{-1} ranges. The midfrequency range of 750−850 cm^{-1} is shown in Figure S6. Figure 5a and b compare key features in the Raman spectrum of CFO and FF-MNS:CFO in the 400−700 cm^{-1} range. The low energy T_{2g} Raman peak in CFO is clearly seen in the pristine sample at 288 cm^{-1}. The presence of FF-MNS Raman peaks in the nanocomposite sample makes it difficult to obtain the peak positions originating only from CFO in the low energy range. The strongest Raman peak in CFO near 680 cm^{-1}, which is the A_{1g} mode, is free from any FF-MNS Raman peaks in that region. This A_{1g} mode observed at 675 cm^{-1} in CFO hardens and shifts to 685 cm^{-1} in FF-MNS:CFO. The shift to higher frequencies (for the Stokes spectrum) in FF-MNS:CFO compared to CFO can be clearly seen upon overlaying the two spectra (Figure S5). The 619 cm^{-1} Raman peak in FF-

DOI: 10.1021/acsanm.7b00344
ACS Appl. Nano Mater. 2018, 1, 1175−1187

Table 1. Peak Positions and Line Widths of C 1s, N 1s, O 1s, and Fe 2p by Fitting the High Resolution XPS Data[a]

orbital	bond	peak position (eV) FF-MNS	FWHM (eV)	peak position (eV) FF-MNS:CFO	FWHM (eV)
C 1s	C−C	284.8	2.26	284.8	2.34
	C−N, C═O	**286.9**	2.33	**286.2**	2.03
	O−C═O	**290.2**	2.41	**288.6**	2.34
N 1s	amide bond −N−C−	**399.9**	5.24	**398.9**	4.54
	amine−NH_3	**402.4**	2.24	**400.9**	2.62
O 1s	C−O	530.3	1.70	530.1	2.42
	lattice oxygen	531.5	2.15	531.6	2.06
	hydroxyl	533.3	2.32	533.6	2.24
	chemisorbed oxygen or from water in the tube	535.6	2.33		
		CFO		FF-MNS:CFO	
Fe $2p_{3/2}$	Fe^{3+} (O_h)	710.2	2.61	710.2	4.79
	Fe^{3+}/Fe^{2+}	**712.8**	4.07	**714.5**	5.44
	satellite peak	717.9	5.54	719.4	6.52
Fe $2p_{1/2}$	Fe^{3+} (O_h)	724.3	4.68	724.3	4.30
	satellite peak	731.8	7.95	732.5	8.66

[a]The numbers in bold signify changes in the binding energy.

MNS:CFO originates from the hexagonal phase of FF-MNS itself. The 458 cm^{-1} Raman peak of CFO also shifts to higher frequencies in FF-MNS:CFO.

The change in the A_{1g} mode frequency position in CFO compared with the nanocomposite sample is an indication of a charge transfer process. The amine group accepts an electron from Fe^{2+} ions (most likely at the O_h site) or Co^{2+} ions, affecting the frequency of the adjacent carboxyl group (discussed in section 3.7). The hardening of the Raman peak position may be further understood based on our XPS results where the binding energy of the Fe $2p_{3/2}$ increases. Since ionic bonds may have some covalent nature, a higher binding energy suggests an enhancement of the stiffness constant for the Fe^{2+}−O bonds, resulting in the hardening of the CFO A_{1g} mode in the nanocomposite sample.

One also observes changes in the FF-MNS Raman frequencies; the 1349 cm^{-1} Raman peak in FF-MNS,[39] which arises from the vibration mode of amide III bond, softens to 1345 cm^{-1} in FF-MNS:CFO. Relative Raman intensities are also affected. In particular, the intensity ratio of the 1434 cm^{-1} to the 1349 cm^{-1} Raman peaks in FF-MNS decreases in the nanocomposite sample, most likely reflecting a change in the torsional angle of the peptide bond. The 1430 cm^{-1} peak in FF-MNS originates from a bending motion of the peptide bond and the amine group, whereas the 1349 cm^{-1} peak arises from a bending of the amine group.

The FTIR data complement the Raman scattering data and yield information on the vibrations originating from the carboxyl and amine groups upon charge transfer. Figure 6a and b show the FTIR spectra of FF-MNS and FF-MNS:CFO in the range from 500 to 4000 cm^{-1}. The frequencies of the amide bonds are shown in c and d. We note that all the absorption peaks in the FTIR spectra are from FF-MNS. The strong vibrations corresponding to the amide group are seen to downshift in energy in FF-MNS:CFO. The 1672 cm^{-1} peak in FF-MNS, which arises from the vibration of amide I (stretching vibration of C═O), shifts to 1668 cm^{-1}, and the 3276 cm^{-1} peak in FF-MNS from the amide A vibration (NH stretching) shifts to 3266 cm^{-1} in FF-MNS:CFO. The amide V (out of plane NH bending) mode at 833 cm^{-1} in FF-MNS shifts to 815 cm^{-1} in FF-MNS:CFO. The downshift of these frequencies in

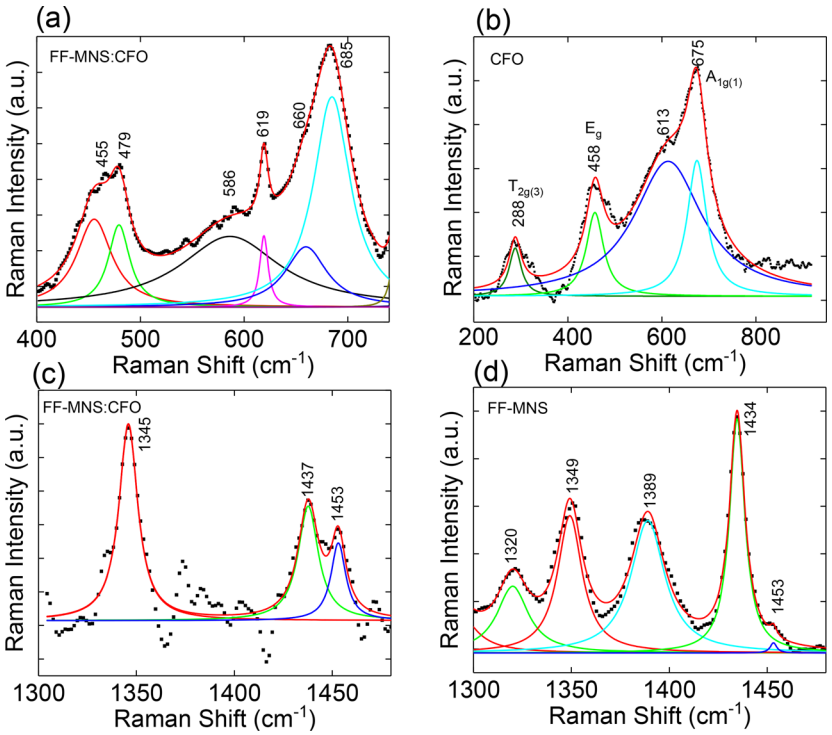

Figure 5. (a and b) Raman spectra of the predominant CFO vibrational modes in FF-MNS:CFO and CFO, respectively. (c and d) The 1300 cm^{-1} region in FF-MNS:CFO and CFO, respectively.

DOI: 10.1021/acsanm.7b00344
ACS Appl. Nano Mater. 2018, 1, 1175−1187

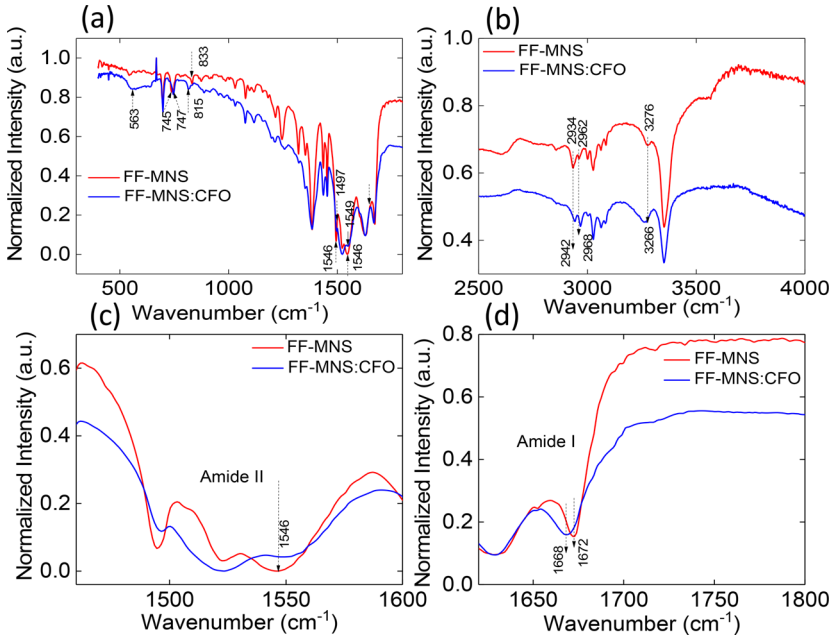

Figure 6. FTIR spectra from FF-MNS and FF-MNS:CFO. The spectra in the range: 500 cm^{-1} to 4000 cm^{-1} are shown in a and b. The high frequency region is shown in b .The region of the amide II and I bonds are shown in c and d, respectively.

the nanocomposite sample may be linked to the XPS data where the binding energy of the C═O and NH_3 bonds decreases, reflecting a decrease in the stiffness constant of the bonds. The trends are less clear for the FTIR peaks that originate from coupled vibrations. One example is the 1546 cm^{-1} peak in FF-MNS, which arises from the amide II bond vibration (associated with coupled C−N stretching and N−H bending vibration), shifting to a higher frequency of 1550 cm^{-1} in FF-MNS:CFO.

Overall, the Raman data highlight changes in CFO frequencies upon binding with FF-MNS, and the FTIR data show changes in the vibrational frequencies associated with the amine and carboxyl groups of FF-MNS. Although the charge transfers from Fe^{2+} and Co^{2+} ions to the amine group, since the carboxyl group is in close proximity to the amine group, the frequency related to the C═O stretching motion is also affected.

3.5. Magnetization. The magnetization data (as a function of the external field (H)) for the powder samples at 300 K are shown in Figure 7. The full magnetization data until 50 kOe are shown in Figure S7. Due to the lack of domains in nanoparticles, the data represent a typical magnetization curve for superparamagnetism with a very low coercive field. Similar magnetization curves (with almost no hysteresis) have also been observed for cobalt iron carbide nanoparticles.[40] The saturation magnetization (M_s) for pure CFO at 5000 Oe is measured as 3.6 μ_B per formula unit (f.u.). Experimentally, we obtain a lower magnetic moment/f.u. compared to the maximum theoretical value of CFO (shown in Table S3) as the measurements were performed at room temperature. We note that FF-MNS:CFO has 20−35% of CFO, confirmed by XRD and XPS. For the magnetization measurements, we assume 35 wt % of CFO in the nanocomposite sample. As shown in Figure 7, M_s for FF-MNS:CFO is 4.6 μ_B/f.u.; compared to CFO, it is an approximately 28% increase in the value of M_s. Using the high field value (Figure S7), the enhancement in M_s is approximately 20% for FF-MNS:CFO. The enhanced value of M_s is an indication that upon binding with FF-MNS, the overall ionic distribution and valency of CFO changes.

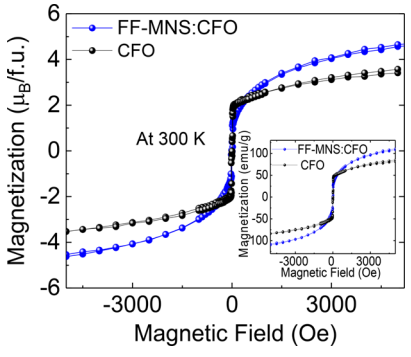

Figure 7. Magnetic hysteresis loops for CFO (black) and FF-MNS:CFO (blue) at room temperature. The inset shows the same data with the unit of magnetization in emu/g.

The magnetization (M) data for both CFO and FF-MNS:CFO follows the modified Langevin function rather than the Langevin function, which is given by[41]

$$M = M_o \mathcal{L}\left(\frac{\mu_p H}{k_B T}\right) + \chi_a H \quad (1)$$

where μ_p is the average magnetic moment per particle, $\mathcal{L}(x) \equiv \coth x - \frac{1}{x}$ is the Langevin function, M_0 is the saturation magnetization, and χ_a is the susceptibility of randomly oriented magnetic particles or any other source of deviation from an ideal magnetic order due to disorder. This behavior has been observed in antiferromagnetic nanoparticles such as ferritin[42] and NiO[43] as well as for magnetic nanocrystals.[44] The need for a modified Langevin function was observed as early as in the late 1930s for colloidal magnetite particles.[45] The fitted data to the modified Langevin

DOI: 10.1021/acsanm.7b00344
ACS Appl. Nano Mater. 2018, 1, 1175−1187

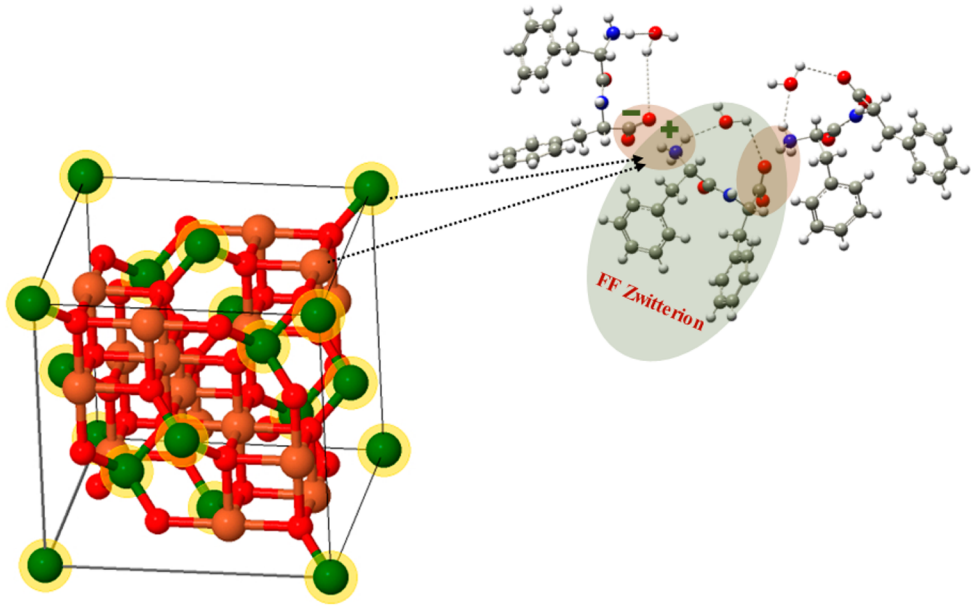

Figure 8. Schematic of the interaction model between CFO and the amine group in FF-MNS.

function are shown in Figure S7, and details of the fit (Table S1) are discussed in the Supporting Information.

Ferromagnetic to antiferromagnetic transition, the coercive field, remnant magnetization, M_s, exchange fields, and the Curie temperatures are known to change in doped CFO compared to pristine CFO.[46−48] An increase in M_s is also seen in CFO/graphene oxide (GFO) nanofibers with increasing GFO content.[49] In the next section, we discuss a few models that explain the behavior of enhanced magnetization in the nanocomposite sample.

3.6. Discussion of Enhanced Magnetic Properties in FF-MNS:CFO. XPS, optical spectroscopy, and magnetization results all point in the direction of a charge transfer mechanism between CFO and FF-MNS. A recent study on the interaction between amino acids and magnetite elucidates its nature, which is governed by the polarity of the side chains and is mediated primarily by the carboxyl groups.[50] Other examples include bonding of CFO particles to p-type carbon nanotubes, which is facilitated through the metal−oxygen bridges, resulting in efficient ion diffusion.[51] In another work on polyaniline (PANI) and CFO, the pyrrolic-N sites play a role.[52]

XPS and Raman scattering both show that Fe/Co−O bonds stiffen in the nanocomposite sample. Further, the magnetization data clearly show an increase in M_s when CFO binds with FF-MNS. Thus, the nature of the charge transfer and the cation redistribution in the nanocomposite is such that there is an overall increase in the magnetic moment. We first show that a few scenarios can be easily ruled out. Since the binding energies related to both Fe and Co increase, and as they are less electronegative than C, N, and O, electrons will be donated from CFO to FF-MNS. Both Fe and Co appear as mixed valence in the CFO crystal structure, and since neither Fe^{4+} nor Co^{4+} can exist in CFO, the only possibilities for a charge transfer would be from Fe^{2+} and Co^{2+}, such that they are oxidized to Fe^{3+} and Co^{3+}. The next question that arises is, which sites, T_d or O_h, are involved? To answer this question, we need to consider both the increase in M_s and changes observed in XPS when CFO binds to FF-MNS.

XRD data show that Co may be occupied both in the T_d as well as in the O_h sites,[53] which is also seen from our Rietveld analysis in Figure S1. Assuming a perfect inverse spinel structure for CFO, our results imply that not all the Fe^{2+} ions in the O_h site are replaced by Co^{2+}. Our Rietveld analysis shows that ∼70% of Co ions are in the O_h site. Unfortunately, solely from single wavelength X-ray analysis, it is difficult to obtain the actual valence states of the ions. Resonance XRD methods using a synchrotron source have been effective for obtaining the mixed valence ratios of Fe^{2+}/Fe^{3+}.[26] We estimate the net magnetic moment per f.u. for different configurations (and spin states) of Fe and Co ions in T_d or O_h positions, shown in Table S3. The crystalline electric field splitting in CFO due to the O_h symmetry is not prominent, so a high spin state is favorable for the d electrons, as also supported by recent experimental findings in Fe_3O_4 as well as in CFO.[54,55]

Shown in Table S3 are two possible situations (one set shown in bold and the other in italics) for enhanced magnetization in FF-MNS:CFO compared to pure CFO. We consider the first model where Fe^{2+} in the O_h site has all been replaced by Co^{2+}, resulting in the configuration of $[Fe^{3+}]_{T_d}[Co^{2+}, Fe^{3+}]_{O_h}O_4$, with a magnetic moment of 3.87 μ_B for CFO. CFO in such a configuration when bound to FF-MNS (in FF-MNS:CFO) is expected to give up an electron, resulting in $[Fe^{3+}]_{T_d}[Co^{3+}Fe^{3+}]_{O_h}O_4$ with a magnetic moment of 4.90 μ_B. In the second model, we assume that Fe^{2+} in the O_h site is not completely replaced by Co^{2+}. With 70% of Co ions in the O_h site (which is close to the Rietveld analysis) and 30% in the T_d site and a 1:2 fraction for Co/Fe (as seen in EDS), we assume a perfect inverse spinel structure with eight ions in the T_d site and 16 ions in the O_h site. These assumptions result in a CFO configuration of $[Fe^{3+}(0.7)Co^{3+}(0.3)]_{T_d}[Fe^{2+}(0.3)$-$Co^{2+}(0.7)Fe^{3+}]_{O_h}O_4$, where the numbers in the bracket denote their fraction, yielding a net magnetic moment of 4.49 μ_B. CFO in such a configuration bound to FF-MNS will change to $[Fe^{3+}(0.7)Co^{3+}(0.3)]_{T_d}[Fe^{3+}(0.3)Co^{3+}(0.7)Fe^{3+}]_{O_h}O_4$ with a net magnetic moment of 5.52 μ_B. Both models show an enhancement in magnetization by 21−23% for FF-MNS:CFO, similar to our experimental observation.

DOI: 10.1021/acsanm.7b00344
ACS Appl. Nano Mater. 2018, 1, 1175−1187

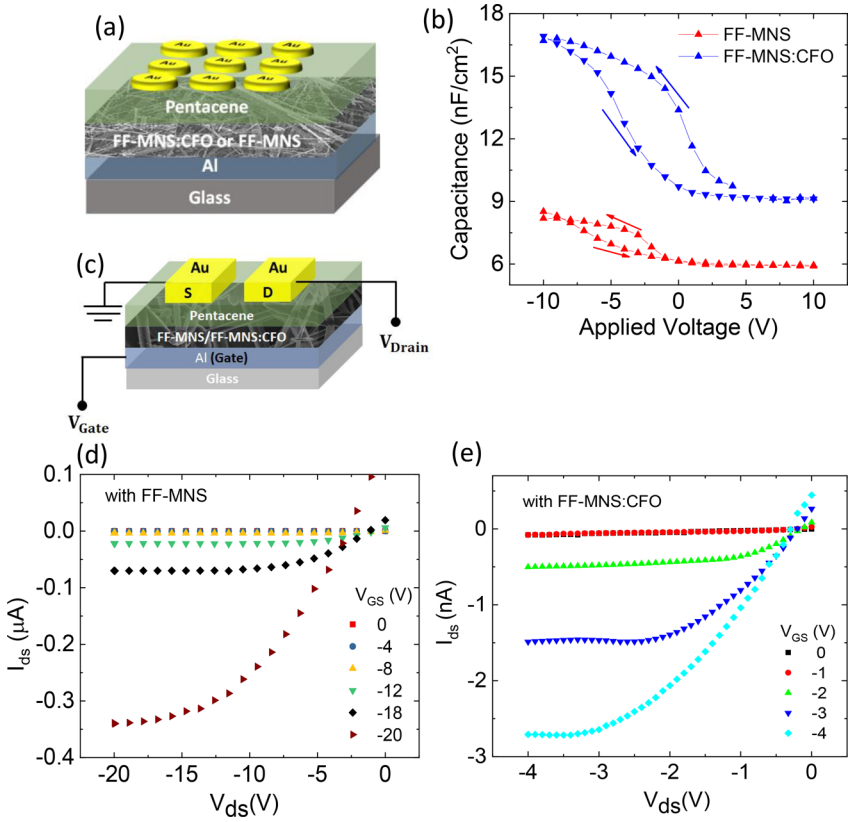

Figure 9. Electrical characteristics of pentacene based MIS capacitors and FETs. FF-MNS and FF-MNS:CFO serve as the dielectric layer. (a) Schematic of MIS structures. (b) C−V characteristics of MIS devices. The arrows denote the sweep directions. (c) Schematic of a bottom-gate, top-contact FET. (d and e) Output characteristics of pentacene FETs using FF-MNS and FF-MNS:CFO as the gate dielectric, respectively. The channel width to length ratio of the FETs was 10.

We note that the above examples are possible outcomes but not a definitive model. The XPS data show a clear increase in binding energy of Fe and Co ion and a downshift in binding energy for the amine and carboxylate bonds. We expect the charge transfer to occur in the amine group of FF-MNS. Shown in Figure 8 is a segment of the FF macrocycle where two neighboring units form a zwitterion; the carboxylic group is negatively charged and the amine group is positively charged. Although the charge transfers to the amine group but since the carboxylic group is connected to it, changes in the vibrational frequencies associated with both groups are expected, as observed in the FTIR spectra. Figure 8 shows a schematic of the Co and Fe ions in the T_d and O_h sites that are most likely involved in the charge transfer process.

3.7. Application of FF-MNS:CFO in Organic Electronics. Organic FETs are being actively developed for applications in large-area flexible electronics.[56,57] Appropriate gate dielectrics that are free of hydroxyl or silanol are necessary for improving charge transport. In order to achieve stable and low-operating voltage FETs, the dielectric surface should be hydrophobic and must provide a relatively high capacitance, which is often a challenge with many polymer dielectrics mainly due to their inherently low dielectric constant. FF-MNS has been successfully used as a dielectric layer, both as a bottom gate and top gate, in pentacene FETs;[5] the nanostructure morphology of FF-MNS was shown to be responsible for withstanding a bias-stress effect. Since CFO has good dielectric properties, we tested the FF-MNS:CFO nanocomposite sample both in pentacene MIS capacitors and in FETs.

Figure 9a shows a schematic of MIS structures with pentacene as the semiconducting layer and FF-MNS or FF-MNS:CFO as the dielectric layer. The C−V curves, in Figure 9b, show a typical p-type behavior with an accumulation of holes at the semiconductor/dielectric interface at a negative bias, a depletion, and a deep depletion region. This is similar to the C−V behavior from MIS capacitors utilizing pentacene and other dielectrics.[58,59] The film thicknesses of FF-MNS and FF-MNS:CFO were approximately the same (550 nm). An increase in the overall capacitance is clearly observed when FF-MNS:CFO is used. Since the film thicknesses of FF-MNS and FF-MNS:CFO were approximately the same, the enhanced capacitance in the nanocomposite sample originates due to the presence of CFO. Hysteresis in C−V curves has various origins due to interface charges and slowly polarizing dipole charges and is typical for polymer dielectric thicknesses greater than 50 nm.[59]

Since organic FETs operate in the accumulation region, the operating voltage depends on the charge density. Given $Q = C_iV_{gs}$, where C_i is the capacitance of the insulator and V_{gs} is the gate-source voltage, a higher value of C_i would imply low operating voltage FETs. To test this, we fabricated pentacene FETs using FF-MNS and FF-MNS:CFO as bottom-gate, top-contact architectures, schematically shown in Figure 9c. A thin layer (<10 nm) of poly(4-vinylphenol) was deposited below the FF-MNS or FF-MNS:CFO layer to reduce the gate leakage current. The output curves (with different gate voltages) from the two FETs are shown in Figure 9d,e; the FF-MNS:CFO based FET shows a lower operating voltage by a factor of 5 compared to the FF-MNS FET. The magnitude of the drain-

DOI: 10.1021/acsanm.7b00344
ACS Appl. Nano Mater. 2018, 1, 1175−1187

source current (I_{ds}) is different due to differences in the leakage current. A study using CFO nanoparticles in a floating gate memory device shows that the average FET carrier mobility is small, mainly due to leakage effects, when the size of the nanoparticles is large; the size of the CFO nanoparticle in this study was varied between 5 and 11 nm.[22] We point out that in our case the size of the CFO nanoparticles is ∼30 nm.

Although the FET application does not exploit the enhanced magnetic properties of CFO in the nanocomposite sample, it provides a general route for lowering operating voltages for other peptide nanostructures or polymer dielectrics to be used as a gate dielectric layer. Moreover, the magnetic properties may provide a potential tuning knob for changing the electrical properties in organic FETs or MIS capacitors in the presence of an external magnetic field. Preliminary insights were obtained by measuring the C−V characteristics from a pentacene FF-MNS:CFO-based MIS capacitor with and without an external magnetic field (Figure S8). An enhanced capacitance is observed in the presence of 0.2 T. Future experiments will fully explore the effect of magnetic field on the electrical properties of FF-MNS:CFO in FET and MIS architectures.

4. CONCLUSIONS

Functionalization of bioinspired peptide nanostructures, FF-MNS, with magnetic nanoparticles of CFO provides an attractive path toward enhancing the magnetic properties. This may find several applications in electronics or in biomedicine where CFO could be contained in a benign environment. The magnetization behavior of both CFO nanoparticles and FF-MNS:CFO follow a modified Langevin-type behavior, characteristic of superparamagnetism. The enhanced saturation magnetization of the nanocomposite sample over pristine CFO sheds insight into the cation distribution and the nature of charge transfer. The inverse spinel structure of CFO with Fe and Co ions both in the O_h and T_d sites provides interaction sites with the amine group in FF-MNS, where either the Co ions or both Fe and Co ions give up an electron to the amine group.

A combination of structural and spectroscopic investigations was performed to probe the mechanism of charge transfer between the peptide nanostructure and CFO. XPS is a sensitive technique for elucidating the oxidation state of elements. An enhancement in the binding energy of Fe $2p_{3/2}$ and Co peaks in FF-MNS:CFO compared to pristine CFO in the XPS spectrum denotes a charge transfer to FF-MNS. The CFO Raman peak at 675 cm^{-1} hardens by almost 10 cm^{-1}; concomitantly the amide I and amide V vibrations in FTIR are seen to soften in FF-MNS:CFO, which is attributed to a charge transfer from Fe^{2+}/Co^{2+} ions to the amine group. Since the carboxyl group is in the proximity of the amine group, the C═O vibrations from FF-MNS in FTIR are also affected.

The dielectric properties of FF-MNS and FF-MNS:CFO were exploited in pentacene MIS capacitors and FETs. A higher value of capacitance in FF-MNS:CFO compared to FF-MNS, observed in MIS capacitors, is responsible for lowering the operating voltages in pentacene FETs. These results have ramifications in low operating voltage floating gate memory FETs. The integration of peptide nanostructures with magnetic nanoparticles opens up a new generation of bioinspired hybrid materials for application in organic electronics. Future strategies will involve functionalizing FF and other short peptides with amphiphilic entities with hydrophobic tails for improving the interaction between self-assembled peptide nanostructures and magnetic nanoparticles.

■ ASSOCIATED CONTENT

Supporting Information

The Supporting Information is available free of charge on the ACS Publications website at DOI: 10.1021/acsanm.7b00344.

Rietveld plot of CFO and FF-MNS CFO; XPS survey spectra of FF-MNS, CFO, and FF-MNS:CFO; EDS spectrum from FF-MNS:CFO; Raman spectra from CFO, FF-MNS, and FF-MNS:CFO in the 200−1600 cm^{-1} range; fits to the magnetization curve by the modified Langevin function; table with magnetic moment from different configures of Fe_3O_4, $CoFe_2O4$, and FF-MNS:CFO; magnetic field dependent capacitance from pentacene MIS capacitors (PDF)

■ AUTHOR INFORMATION

Corresponding Author

*E-mail: guhas@missouri.edu.

ORCID

Fabio F. Ferreira: 0000-0003-1516-1221

Suchismita Guha: 0000-0002-6269-2298

Author Contributions

The manuscript was written through contributions of all authors. All authors have given approval to the final version of the manuscript.

Notes

The authors declare no competing financial interest.

■ ACKNOWLEDGMENTS

We acknowledge the support of this work through the University of Missouri Research Board grant and the U.S. National Science Foundation under grant no. ECCS-1707588. F.F.F. acknowledges the financial support provided by CNPq (grants # 402289/2013-7 and 307664/2015-5). We thank Dr. Xiaoqing He at the Electron Microscopy Core in MU for help with the SEM/TEM images and Amrit Laudari for the fabrication of transistors.

■ REFERENCES

(1) Tao, K.; Makam, P.; Aizen, R.; Gazit, E. Self-Assembling Peptide Semiconductors. *Science* **2017**, *358*, eaam9756.

(2) Kol, N.; Adler-Abramovich, L.; Barlam, D.; Shneck, R. Z.; Gazit, E.; Rousso, I. Self-Assembled Peptide Nanotubes Are Uniquely Rigid Bioinspired Supramolecular Structures. *Nano Lett.* **2005**, *5*, 1343−1346.

(3) Liberato, M. S.; Kogikoski, S.; da Silva, E. R.; de Araujo, D. R.; Guha, S.; Alves, W. A. Polycaprolactone Fibers with Self-Assembled Peptide Micro/Nanotubes: A Practical Route Towards Enhanced Mechanical Strength and Drug Delivery Applications. *J. Mater. Chem. B* **2016**, *4*, 1405−1413.

(4) Ryu, J.; Park, C. B. High Stability of Self-Assembled Peptide Nanowires against Thermal, Chemical, and Proteolytic Attacks. *Biotechnol. Bioeng.* **2010**, *105*, 221−230.

(5) Cipriano, T.; Knotts, G.; Laudari, A.; Bianchi, R. C.; Alves, W. A.; Guha, S. Bioinspired Peptide Nanostructures for Organic Field-Effect Transistors. *ACS Appl. Mater. Interfaces* **2014**, *6*, 21408−21415.

(6) Khanra, S.; Cipriano, T.; Lam, T.; White, T. A.; Fileti, E. E.; Alves, W. A.; Guha, S. Self-Assembled Peptide−Polyfluorene Nanocomposites for Biodegradable Organic Electronics. *Adv. Mater. Interfaces* **2015**, *2*, 1500265−1500274.

(7) Gorbitz, C. H. The Structure of Nanotubes Formed by Diphenylalanine, the Core Recognition Motif of Alzheimer's [Small Beta]-Amyloid Polypeptide. *Chem. Commun.* **2006**, 2332−2334.
(8) Silva, R. F.; Araújo, D. R.; Silva, E. R.; Ando, R. A.; Alves, W. A. L-Diphenylalanine Microtubes as a Potential Drug-Delivery System: Characterization, Release Kinetics, and Cytotoxicity. *Langmuir* **2013**, *29*, 10205−10212.
(9) Reches, M.; Gazit, E. Molecular Self-Assembly of Peptide Nanostructures: Mechanism of Association and Potential Uses. *Curr. Nanosci.* **2006**, *2*, 105−111.
(10) Pandey, G.; Saikia, J.; Sasidharan, S.; Joshi, D. C.; Thota, S.; Nemade, H. B.; Chaudhary, N.; Ramakrishnan, V. Modulation of Peptide Based Nano-Assemblies with Electric and Magnetic Fields. *Sci. Rep.* **2017**, *7*, 2726−2735.
(11) Li, J.; He, Q.; Yan, X. *Molecular Assembly of Biomimetic Systems*; Wiley: 2010.
(12) Martins, T. D.; de Souza, M. I.; Cunha, B. B.; Takahashi, P. M.; Ferreira, F. F.; Souza, J. A.; Fileti, E. E.; Alves, W. A. Influence of Ph and Pyrenyl on the Structural and Morphological Control of Peptide Nanotubes. *J. Phys. Chem. C* **2011**, *115*, 7906−7913.
(13) Souza, M. I.; Jaques, Y. M.; de Andrade, G. P.; Ribeiro, A. O.; da Silva, E. R.; Fileti, E. E.; Avilla, E. d. S.; Pinheiro, M. V.; Krambrock, K.; Alves, W. A. Structural and Photophysical Properties of Peptide Micro/Nanotubes Functionalized with Hypericin. *J. Phys. Chem. B* **2013**, *117*, 2605−2614.
(14) Vertegel, A. A.; Siegel, R. W.; Dordick, J. S. Silica Nanoparticle Size Influences the Structure and Enzymatic Activity of Adsorbed Lysozyme. *Langmuir* **2004**, *20*, 6800−6807.
(15) Su, Y.; He, Q.; Yan, X.; Fei, J.; Cui, Y.; Li, J. Peptide Mesocrystals as Templates to Create an Au Surface with Stronger Surface-Enhanced Raman Spectroscopic Properties. *Chem. - Eur. J.* **2011**, *17*, 3370−3375.
(16) Kogikoski, S.; Khanra, S.; Alves, W. A.; Guha, S. Sers Active Self-Assembled Diphenylalanine Micro/Nanostructures: A Combined Experimental and Theoretical Investigation. *J. Chem. Phys.* **2017**, *147*, 084703.
(17) Maaz, K.; Mumtaz, A.; Hasanain, S. K.; Ceylan, A. Synthesis and Magnetic Properties of Cobalt Ferrite ($CoFe_2O_4$) Nanoparticles Prepared by Wet Chemical Route. *J. Magn. Magn. Mater.* **2007**, *308*, 289−295.
(18) Jun, Y.-w.; Seo, J.-w.; Cheon, J. Nanoscaling Laws of Magnetic Nanoparticles and Their Applicabilities in Biomedical Sciences. *Acc. Chem. Res.* **2008**, *41*, 179−189.
(19) Sanpo, N.; Berndt, C. C.; Wen, C.; Wang, J. Transition Metal-Substituted Cobalt Ferrite Nanoparticles for Biomedical Applications. *Acta Biomater.* **2013**, *9*, 5830−5837.
(20) Amiri, S.; Shokrollahi, H. The Role of Cobalt Ferrite Magnetic Nanoparticles in Medical Science. *Mater. Sci. Eng., C* **2013**, *33*, 1−8.
(21) Pašukonienė, V.; Mlynska, A.; Steponkienė, S.; Poderys, V.; Matulionytė, M.; Karabanovas, V.; Statkutė, U.; Purvinienė, R.; Kraśko, J. A.; Jagminas, A.; Kurtinaitienė, M.; Strioga, M.; Rotomskis, R. Accumulation and Biological Effects of Cobalt Ferrite Nanoparticles in Human Pancreatic and Ovarian Cancer Cells. *Medicina (Kaunas, Lithuania)* **2014**, *50*, 237−244.
(22) Jung, J. H.; Kim, S.; Kim, H.; Park, J.; Oh, J. H. High-Performance Flexible Organic Nano-Floating Gate Memory Devices Functionalized with Cobalt Ferrite Nanoparticles. *Small* **2015**, *11*, 4976−4984.
(23) Ryu, J.; Kim, S.-W.; Kang, K.; Park, C. B. Synthesis of Diphenylalanine/Cobalt Oxide Hybrid Nanowires and Their Application to Energy Storage. *ACS Nano* **2010**, *4*, 159−164.
(24) Gazit, E. Self-Assembled Peptide Nanostructures: The Design of Molecular Building Blocks and Their Technological Utilization. *Chem. Soc. Rev.* **2007**, *36*, 1263−1269.
(25) Andrade-Filho, T.; Martins, T. C.; Ferreira, F. F.; Alves, W. A.; Rocha, A. R. Water-Driven Stabilization of Diphenylalanine Nanotube Structures. *Theor. Chem. Acc.* **2016**, *135*, 185.
(26) Ferreira, F. F.; Bueno, P. R.; Setti, G. O.; Giménez-Romero, D.; García-Jareño, J. J.; Vicente, F. Resonant X-Ray Diffraction as a Tool to Calculate Mixed Valence Ratios: Application to Prussian Blue Materials. *Appl. Phys. Lett.* **2008**, *92*, 264103.
(27) Rietveld, H. M. Line Profiles of Neutron Powder-Diffraction Peaks for Structure Refinement. *Acta Crystallogr.* **1967**, *22*, 151−152.
(28) Rietveld, H. M. A Profile Refinement Method for Nuclear and Magnetic Structures. *J. Appl. Crystallogr.* **1969**, *2*, 65−71.
(29) Toby, B. H. R Factors in Rietveld Analysis: How Good Is Good Enough? *Powder Diffr.* **2006**, *21*, 67−70.
(30) Bianchi, R. C.; da Silva, E. R.; Dall'Antonia, L. H.; Ferreira, F. F.; Alves, W. A. A Nonenzymatic Biosensor Based on Gold Electrodes Modified with Peptide Self-Assemblies for Detecting Ammonia and Urea Oxidation. *Langmuir* **2014**, *30*, 11464−11473.
(31) Hill, R. J.; Howard, C. J. Quantitative Phase Analysis from Neutron Powder Diffraction Data Using the Rietveld Method. *J. Appl. Crystallogr.* **1987**, *20*, 467−474.
(32) Sun, H.; Yang, X.; Zhao, L.; Xu, T.; Lian, J. One-Pot Hydrothermal Synthesis of Octahedral $CoFe/CoFe_2O_4$ Submicron Composite as Heterogeneous Catalysts with Enhanced Peroxymonosulfate Activity. *J. Mater. Chem. A* **2016**, *4*, 9455−9465.
(33) Gu, Z.; Xiang, X.; Fan, G.; Li, F. Facile Synthesis and Characterization of Cobalt Ferrite Nanocrystals Via a Simple Reduction−Oxidation Route. *J. Phys. Chem. C* **2008**, *112*, 18459−18466.
(34) Pradhan, D. K.; Kumari, S.; Puli, V. S.; Das, P. T.; Pradhan, D. K.; Kumar, A.; Scott, J. F.; Katiyar, R. S. Correlation of Dielectric, Electrical and Magnetic Properties near the Magnetic Phase Transition Temperature of Cobalt Zinc Ferrite. *Phys. Chem. Chem. Phys.* **2017**, *19*, 210−218.
(35) Egelhoff, W. F. Core-Level Binding-Energy Shifts at Surfaces and in Solids. *Surf. Sci. Rep.* **1987**, *6*, 253−415.
(36) Hosterman, B. D.; Farley, J. W.; Johnson, A. L. Spectroscopic Study of the Vibrational Modes of Magnesium Nickel Chromite. *J. Phys. Chem. Solids* **2013**, *74*, 985−990.
(37) Lekprasert, B.; Korolkov, V.; Falamas, A.; Chis, V.; Roberts, C. J.; Tendler, S. J. B.; Notingher, I. Investigations of the Supramolecular Structure of Individual Diphenylalanine Nano- and Microtubes by Polarized Raman Microspectroscopy. *Biomacromolecules* **2012**, *13*, 2181−2187.
(38) Khanra, S.; Ghosh, K.; Ferreira, F. F.; Alves, W. A.; Punzo, F.; Yu, P.; Guha, S. Probing Nonlinear Optical Coefficients in Self-Assembled Peptide Nanotubes. *Phys. Chem. Chem. Phys.* **2017**, *19*, 3084−3093.
(39) Rygula, A.; Majzner, K.; Marzec, K. M.; Kaczor, A.; Pilarczyk, M.; Baranska, M. Raman Spectroscopy of Proteins: A Review. *J. Raman Spectrosc.* **2013**, *44*, 1061−1076.
(40) El-Gendy, A. A.; Bertino, M.; Clifford, D.; Qian, M.; Khanna, S. N.; Carpenter, E. E. Experimental Evidence for the Formation of Cofe2c Phase with Colossal Magnetocrystalline-Anisotropy. *Appl. Phys. Lett.* **2015**, *106*, 213109.
(41) Seehra, M. S.; Babu, V. S.; Manivannan, A.; Lynn, J. W. Neutron Scattering and Magnetic Studies of Ferrihydrite Nanoparticles. *Phys. Rev. B: Condens. Matter Mater. Phys.* **2000**, *61*, 3513−3518.
(42) Makhlouf, S. A.; Parker, F. T.; Berkowitz, A. E. Magnetic Hysteresis Anomalies in Ferritin. *Phys. Rev. B: Condens. Matter Mater. Phys.* **1997**, *55*, R14717−R14720.
(43) Tiwari, S. D.; Rajeev, K. P. Effect of Distributed Particle Magnetic Moments on the Magnetization of Nio Nanoparticles. *Solid State Commun.* **2012**, *152*, 1080−1083.
(44) Dutta, P.; Manivannan, A.; Seehra, M. S.; Shah, N.; Huffman, G. P. Magnetic Properties of Nearly Defect-Free Maghemite Nanocrystals. *Phys. Rev. B: Condens. Matter Mater. Phys.* **2004**, *70*, 174428.
(45) Elmore, W. C. The Magnetization of Ferromagnetic Colloids. *Phys. Rev.* **1938**, *54*, 1092−1095.
(46) Ramana, C. V.; Kolekar, Y. D.; Kamala Bharathi, K.; Sinha, B.; Ghosh, K. Correlation between Structural, Magnetic, and Dielectric Properties of Manganese Substituted Cobalt Ferrite. *J. Appl. Phys.* **2013**, *114*, 183907.

DOI: 10.1021/acsanm.7b00344
ACS Appl. Nano Mater. 2018, 1, 1175−1187

(47) Paulsen, J. A.; Ring, A. P.; Lo, C. C. H.; Snyder, J. E.; Jiles, D. C. Manganese-Substituted Cobalt Ferrite Magnetostrictive Materials for Magnetic Stress Sensor Applications. *J. Appl. Phys.* **2005**, *97*, 044502.
(48) Melikhov, Y.; Snyder, J. E.; Jiles, D. C.; Ring, A. P.; Paulsen, J. A.; Lo, C. C. H.; Dennis, K. W. Temperature Dependence of Magnetic Anisotropy in Mn-Substituted Cobalt Ferrite. *J. Appl. Phys.* **2006**, *99*, 08R102.
(49) Eid, C.; Assaf, E.; Habchi, R.; Miele, P.; Bechelany, M. Tunable Properties of Go-Doped $CoFe_2O_4$ Nanofibers Elaborated by Electrospinning. *RSC Adv.* **2015**, *5*, 97849−97854.
(50) Schwaminger, S. P.; García, P. F.; Merck, G. K.; Bodensteiner, F. A.; Heissler, S.; Günther, S.; Berensmeier, S. Nature of Interactions of Amino Acids with Bare Magnetite Nanoparticles. *J. Phys. Chem. C* **2015**, *119*, 23032−23041.
(51) Wang, L.; Zhuo, L.; Cheng, H.; Zhang, C.; Zhao, F. Porous Carbon Nanotubes Decorated with Nanosized Cobalt Ferrite as Anode Materials for High-Performance Lithium-Ion Batteries. *J. Power Sources* **2015**, *283*, 289−299.
(52) Xiong, P.; Chen, Q.; He, M.; Sun, X.; Wang, X. Cobalt Ferrite-Polyaniline Heteroarchitecture: A Magnetically Recyclable Photocatalyst with Highly Enhanced Performances. *J. Mater. Chem.* **2012**, *22*, 17485−17493.
(53) Rieck, G. D.; Thijssen, J. J. M. The Cation Distribution in $CoFe_2O_4$. *Acta Crystallogr., Sect. B: Struct. Crystallogr. Cryst. Chem.* **1968**, *24*, 982−983.
(54) Sinha, A. K.; Singh, M. N.; Achary, S. N.; Sagdeo, A.; Shukla, D. K.; Phase, D. M. Crystal Field Splitting and Spin States of Co Ions in Cobalt Ferrite with Composition $Co_{1.5}Fe_{1.5}O_4$ Using Magnetization and X-Ray Absorption Spectroscopy Measurements. *J. Magn. Magn. Mater.* **2017**, *435*, 87−95.
(55) Bengtson, A.; Morgan, D.; Becker, U. Spin State of Iron in Fe_3O_4 Magnetite and H-Fe_3O_4. *Phys. Rev. B: Condens. Matter Mater. Phys.* **2013**, *87*, 155141.
(56) Rogers, J. A.; Bao, Z.; Baldwin, K.; Dodabalapur, A.; Crone, B.; Raju, V. R.; Kuck, V.; Katz, H.; Amundson, K.; Ewing, J.; Drzaic, P. Paper-Like Electronic Displays: Large-Area Rubber-Stamped Plastic Sheets of Electronics and Microencapsulated Electrophoretic Inks. *Proc. Natl. Acad. Sci. U. S. A.* **2001**, *98*, 4835−4840.
(57) Sekitani, T.; Someya, T. Stretchable, Large-Area Organic Electronics. *Adv. Mater.* **2010**, *22*, 2228−2246.
(58) Ukah, N. B.; Granstrom, J.; Sanganna Gari, R. R.; King, G. M.; Guha, S. Low-Operating Voltage and Stable Organic Field-Effect Transistors with Poly (Methyl Methacrylate) Gate Dielectric Solution Deposited from a High Dipole Moment Solvent. *Appl. Phys. Lett.* **2011**, *99*, 243302.
(59) Ukah, N. B.; Senanayak, S. P.; Adil, D.; Knotts, G.; Granstrom, J.; Narayan, K. S.; Guha, S. Enhanced Mobility and Environmental Stability in All Organic Field-Effect Transistors: The Role of High Dipole Moment Solvent. *J. Polym. Sci., Part B: Polym. Phys.* **2013**, *51*, 1533−1542.

DOI: 10.1021/acsanm.7b00344
ACS Appl. Nano Mater. 2018, 1, 1175−1187